Soft Matter

Micropattern-controlled wicking enhancement in hierarchical micro/nanostructures

Journal:	*Soft Matter*
Manuscript ID	SM-ART-05-2019-001055.R2
Article Type:	Paper
Date Submitted by the Author:	11-Jul-2019
Complete List of Authors:	Rokoni, Arif; Drexel University, Mechanical Engineering and Mechanics Kim, Dong-ook; Drexel University, Mechanical Engineering and Mechanics Sun, Ying; Drexel University, Mechanical Engineering and Mechanics

Micropattern-controlled wicking enhancement in hierarchical micro/nanostructures

Arif Rokoni, Dong-Ook Kim, and Ying Sun*

Department of Mechanical Engineering and Mechanics, Drexel University, Philadelphia, PA 19104, USA

Abstract

Wicking in hierarchical micro/nanostructured surfaces has gained significant attention due to its potential applications in thermal management, moisture capturing, drug delivery, and oil recovery. While some studies have shown that hierarchical structures enhance wicking over micro-structured surfaces, others have found very limited wicking improvement. In this study, we demonstrate the importance of micropatterns on wicking enhancement in hierarchical surfaces using ZnO nanorods grown on silicon micropillars of varying spacings and heights. The wicking front over hierarchical surfaces is found to follow a two-stage motion, where wicking is faster around micropillars, but slower in between adjacent pillar rows and the latter stage dictates the wicking enhancement in hierarchical surfaces. The competition between the added capillary action and friction due to nanostructures in these two different wicking stages results in a strong dependence of wicking enhancement on the height and spacing of the micropillars. A scaling model for the propagation coefficient is developed for wicking in hierarchical surfaces considering nanostructures in both wicking stages and the model agrees well with the experiments. This microstructure-controlled two-stage wicking characteristic sheds light on a more effective design of hierarchical micro/nanostructured surfaces for wicking enhancement.

* Corresponding author. Tel.: +1(215)895-1373; Fax: +1(215)895-1478; E-mail:ys347@drexel.edu.

1. Introduction

Wicking on textured surfaces has gained significant attention due to its numerous applications in nature and engineered systems such as thermal management,[1-6] moisture capturing,[7-8] drug delivery,[9-10] biomedical devices[11-14] and oil recovery.[15] Near a century ago, Washburn predicted the dynamics of liquid imbibition into capillary tubes, driven by the surface tension force, where the imbibition length is proportional to the square root of time.[16] Recent developments[1, 6, 15, 17-27] in fabrication processes of micro, nano and hierarchical surfaces have created ample opportunities to tune the topography of the structured surfaces to achieve different wicking conditions. Meanwhile, several models have been developed to extend the classic Washburn model for a variety of engineered surfaces.

Bico et al.[28] extended the Washburn model for wicking dynamics in capillary tubes to surfaces with micropillars by introducing an empirical parameter β to account for the added viscous resistance due to micropillars. Ishino et al.[29] distinguished wicking on micropillar surfaces into short and long-pillar scenarios, where the viscous resistance from pillar sidewalls is ignored for short pillars whereas the pillar base resistance is neglected for long pillars. Using Surface Evolver (SE)[30] to predict the 3D meniscus shape and the 1D Brinkman's equation to approximate the viscous resistance, Xiao et al.[31] proposed a semi-analytical model to predict the liquid propagation rate on surfaces with micropillar arrays. Mai et al.[20] correlated the viscous resistance enhancement factor β with the pillar height-to-spacing ratio by simplifying the pillars as channels having the same porosity and validated the model by wicking experiments on surfaces with nanopillar arrays. Interestingly, recent boiling experiments[32] have observed delays in the undesirable Leidenfrost effect on surfaces with sparse micropillars, where the liquid wicking rate is found to be overpredicted by using the above mentioned models. A recent study by Kim et al.[33] considered

cases with pillar spacing ranging from dense to sparse and identified a two-stage wicking motion for sparse pillars where wicking is faster around pillars but slower in between pillar rows. The slow wicking stage between pillar rows is mainly due to its smaller pre-wet surface area per wicking length, resulting in a weaker driving force in the system free energy. A scaling model relating the propagation coefficient with fluid properties and micropillar geometries has been proposed, where the propagation coefficient for sparse pillars is smaller compared to dense pillars while keeping other parameters the same.[33]

Recently, wicking enhancements have been reported by adding nanostructures to microstructures for creating hierarchical surfaces that are superhydrophilic in an effort to enhance the critical heat flux of pool boiling and thin film evaporation.[1, 6, 19, 34-38] While others have found that the low permeability of the added nanostructures, as compared to microstructures alone, limits their role in assisting bulk wicking, resulting in a negligible wicking improvement.[2] For example, the added viscous resistance becomes important when the height of the ZnO nanorods approaches half of the micropillar spacing for hierarchical surfaces consisting of ZnO nanorods on micropillars of varying heights.[21] Despite of these studies, the general guidelines of predicting the wicking enhancement in hierarchical surfaces of two very different length scales have yet to be discovered.

In this study, the wicking dynamics of hierarchical micro/nanostructured surfaces is examined by conducting systematic wicking experiments using ZnO nanorods grown on silicon micropillars of varying spacings and heights. A two-stage wicking motion is observed on hierarchical surfaces, where wicking is faster while around micropillars but slower in between pillar rows. The role of nanostructure is different in these two stages, where no obvious wicking enhancement is observed with nanostructures in the first stage, but significant enhancement is found during the second stage where wicking is slower in-between micropillar rows and this second stage dictates the bulk

wicking dynamics. Wicking improvement in hierarchical structures over bare micropillar surfaces is found to depend on the spacing and height of the micropillars. A new scaling model relating the propagation coefficient to the fluid properties and geometrical parameters of the hierarchical surfaces is proposed, considering nanostructures in both wicking stages. The model predictions are compared with our wicking experiments.

2. Experimental methods

In this study, circular micropillars were fabricated using deep reactive ion etching (DRIE) of silicon (100) wafers where the etching time was controlled to create micropillars of different heights. The resulting micropillar diameter is fixed at 10 μm, the center-to-center spacing varies from 30 μm to 60 μm, and the height varies from 8 μm to 26 μm. To create a hierarchical surface, ZnO nanorods were grown on bare silicon micropillars with 25 mm×25 mm sample dimensions using a chemical process,[39] where the growth time and concentration of reactants determine the height and diameter of the ZnO nanorods. The nanoscale roughness, r_n, is determined using $r_n = 1 + \frac{ph_n}{l^2}$, where p is the total perimeter of all nanorods within a square window of length l of the nanostructure base plane and h_n is the effective height of the nanorods. The same growth time of 4 hours and concentrations of Hexamethylenetetramine (HMT) and Zinc nitrate (1:1) at 0.04M were used, and hence the identical roughness of the ZnO nanorods was kept for the hierarchical surfaces. Whereas the growth time varied from 2 to 5 hours and the concentrations of HMT and Zinc nitrate (1:1) varied from 0.01M to 0.05M for the nanorod-only cases, resulting in different nanoscale roughness values shown in the Supplemental Material. Figure 1 shows the scanning electron microscopy (SEM) images of fabricated micropillar (Fig. 1a and 1b) and hierarchical (Fig.

1c and 1d) surfaces. The growth time of 4 hours yields a nanorod height of ≈1 μm, but an effective height of ≈350 nm contributes to wicking due to closely packed nanorods near the base plane (see the SEM image shown in Fig. 1d). For the ZnO nanorod diameter of ≈30 nm and effective height of ≈350 nm, the corresponding nanoscale roughness of $r_n \approx 2.5$ is assumed in the model for hierarchical surfaces, determined based on top- and side-view SEM images of nanorods.

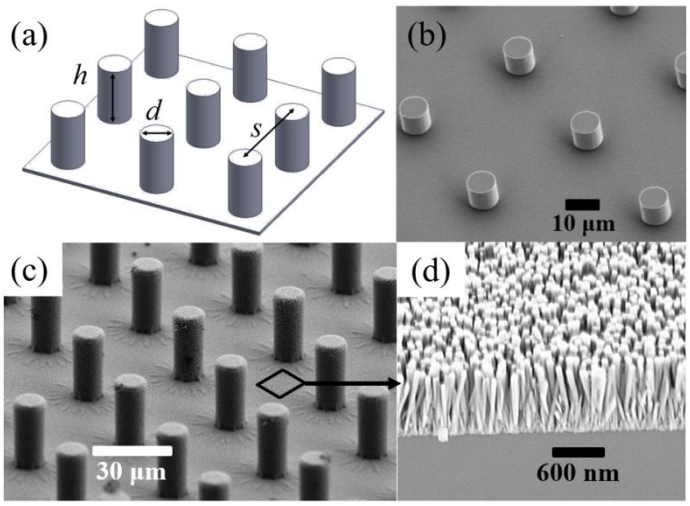

Figure 1. (a) Schematic of a micropillar surface, showing pillar diameter *d*, height *h* and center-to-center spacing *s*. SEM images of (b) silicon micropillars, (c) a hierarchical micro/nanostructured surface, and (d) ZnO nanorods on the base plane of the micropillar array.

To minimize the effects of inertia during wicking, a vertical wicking mechanism[31] is applied in this study. Figure 2a shows the schematic of the wicking test setup. The substrate was placed vertically in a deionized (DI) water bath and the wicking dynamics was captured via a high-speed camera (Phantom V711) at a frame rate of 6,000 frames per second using a 20× objective with a spatial resolution of 1 micron/pixel. A high-powered LED light (Thorlabs, Solis-445C) and a beam splitter were used for illumination. Substrate surfaces were cleaned with isopropyl alcohol (IPA) and acetone, rinsed with DI water, and followed by air plasma cleaning (18 W and 250 mTorr,

Harrick Plasma PDC-32G). The wettability of pure silicon and ZnO nanofilm coated silicon[40] after 4 minutes of plasma cleaning is experimentally determined using interferometry imaging of a drop contact line region. An intrinsic water contact angle of $\theta \approx 4^{\circ}$ was obtained for pure silicon and $\theta \approx 5^{\circ}$ for ZnO nanofilm coated silicon. The intrinsic contact angle remains the same for about 1 hour and then gradually increases. Thus, all wicking tests were done within 5 mins of plasma cleaning to ensure a constant intrinsic contact angle. Figure 2b shows a snapshot of the wicking process, where the water level and wicking front are marked with arrows. The instantaneous wicking length, the distance of the wicking front from the water bath, is obtained by averaging at three different positions, equally spaced within the field of view of ≈ 10 mm, perpendicular to the wicking direction. Each test is repeated five times to account for the imperfect flatness of the wicking front. Consider the wicking length, a, scales with time to the power n, i.e., $a = Gt^n$, where n is the wicking index (n = 0.5 in the Washburn model) and G is the propagation coefficient. In this study, the wicking indexes for both microstructures alone and hierarchical surfaces have been found to be close to 0.5, as described in Supplemental Materials.

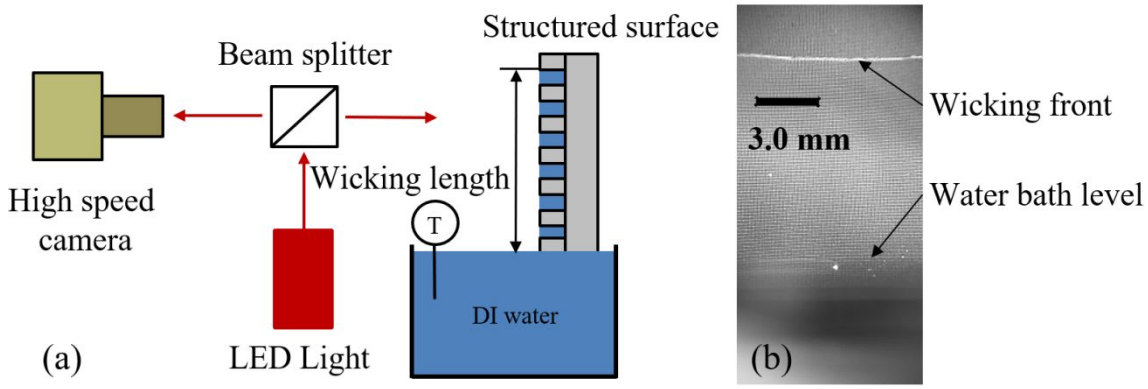

Figure 2. (a) Schematic of the vertical wicking test, where a high-speed camera is used to record the instantaneous wicking front location on structured surfaces. (b) Snapshot of wicking over structured surface showing the instantaneous wicking front and the water bath level, which is the position of wicking front at t = 0 s.

3. Experimental results

To understand the wicking dynamics of hierarchical surfaces, the comparison of wicking in micropillars with and without nanorods has been conducted. The wicking dynamics of micropillar-only surfaces of varying pillar height and spacing compared with existing wicking models are summarized in Supplemental Material. Figure 3 shows the snapshots of wicking front positions over time as water wicks over micropillars of different diameter-to-spacing ratios without (left panel) and with (right panel) nanorods, where Fig. 3a is for diameter-to-spacing ratio, *d/s*, of 0.333 and Fig. 3b is for *d/s* of 0.2, both at the micropillar height of 13 μm. Here, $t = 0$ is when the structured surface touches the DI water and water starts to wick vertically from the initial wicking front position marked by a red dashed line. No significant wicking improvement is observed due to the presence of nanostructures for micropillar *d/s* of 0.333 as shown in Fig 3a. However, wicking is much faster for hierarchical surfaces compared to the bare micropillar case at $d/s = 0.2$ shown in Fig. 3b. Note that, the diameter-to-spacing ratio is varied by changing the spacing between micropillars while keeping the pillar diameter fixed at 10 μm such that a lower diameter-to-spacing ratio corresponds to a larger pillar spacing and a sparser pillar array.

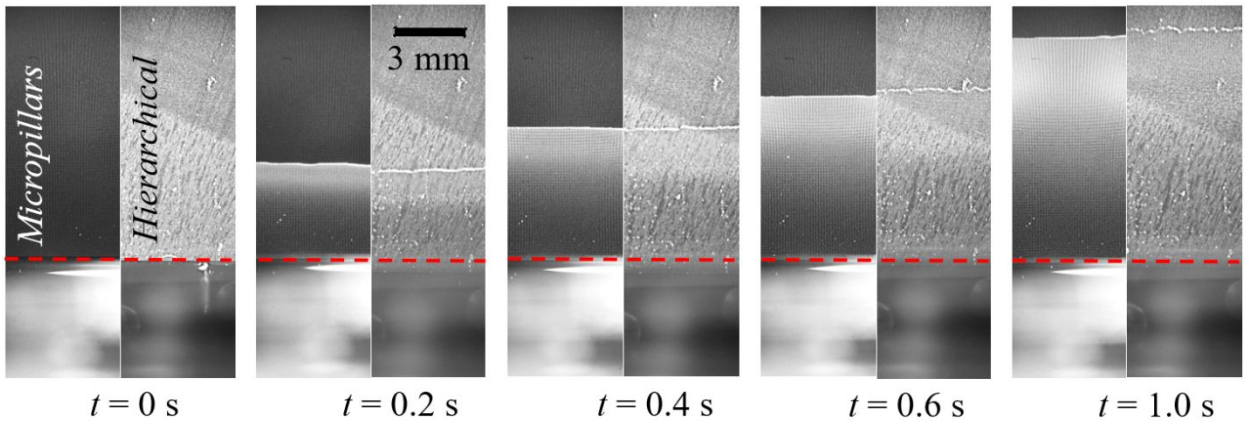

(a) *d/s* =0.333

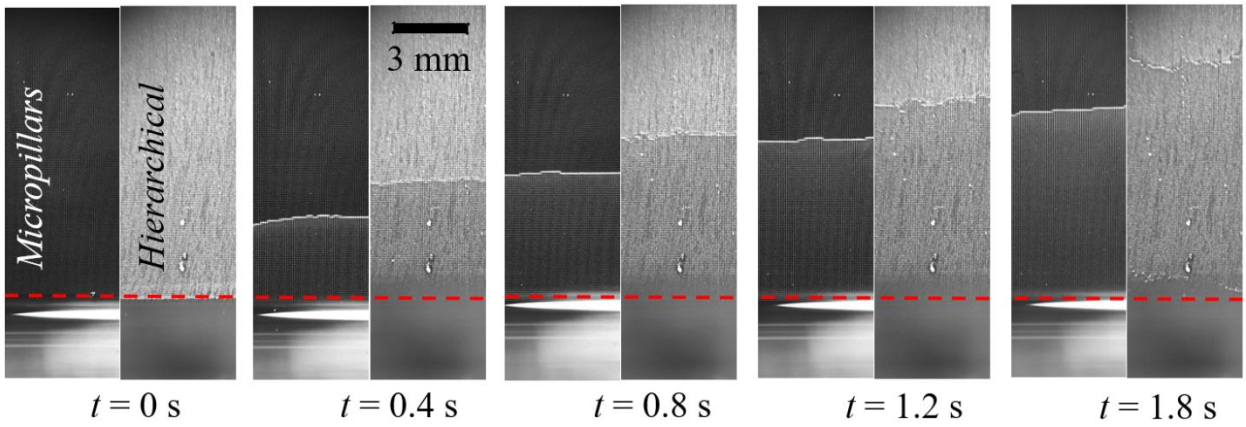

(b) *d/s* =0.2

Figure 3. Wicking dynamics of DI water over micropillar and hierarchical micro/nanostructured surfaces for micropillar diameter-to-spacing ratios of (a) *d/s* =0.333 and (b) *d/s* =0.2. No significant wicking improvement due to nanostructures is observed for the *d/s* =0.333 case but observable enhancement is found for *d/s* =0.2. Initial wicking front position is marked with a red dashed line. For all cases, the pillar height is kept at h = 13 μm.

Figure 4 shows the quantitative comparison of the wicking length over time for micropillars without (black squares) and with (red squares) nanorods for the cases shown in Fig. 3. Each experiment was repeated 5 times and the solid lines in Fig. 4 are power-law fittings assuming the wicking index n = 0.5. For *d/s* = 0.333, the propagation coefficients, G, from curve fitting are

8.198 and 8.576 mm/s$^{1/2}$ without and with nanorods, respectively, with only a 4.6% increase in G due to added nanostructures, very close to the error bar of 4.1% for micropillars. Whereas a more obvious wicking enhancement without and with nanostructure has been observed for the d/s = 0.2 case, as shown in Fig. 4b, where the propagation coefficients, G, are 4.505 and 5.697 mm/s$^{1/2}$, respectively, a 26% increase due to nanostructures. Note that the wicking length measurement is limited to 10 mm due to the camera field of view. It is also important to note that, the nanostructure roughness of ≈2.5 is kept the same for both micropillar diameter-to-spacing ratios whereas very different wicking enhancements are achieved with and without nanostructures at these two d/s values, indicating that microstructure geometries play an important role in wicking enhancement of hierarchical surfaces.

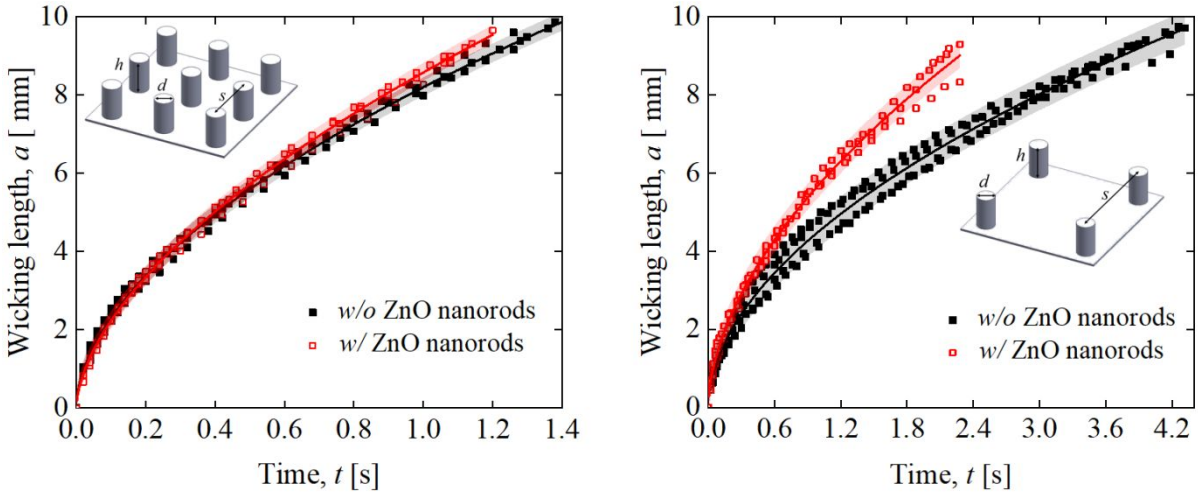

Figure 4. Experimental wicking length over time for bare micropillars (black square) and hierarchical surfaces (red square) for different micropillar diameter-to-spacing ratios: (a) d/s =0.333 and (b) d/s =0.2 both at pillar height h = 13 μm. Solid lines are power-law fittings using data from all five experiments assuming the wicking index n = 0.5. Shaded areas correspond to the 90% prediction band.

To obtain an in-depth understanding of how wicking improvement of hierarchical surfaces depends on micropillar geometries, the wicking dynamics was observed at the individual

micropillar level using 20× zoom lens. Figure 5c shows the instantaneous wicking front positions over time for both micropillar and hierarchical surfaces for micropillar diameter-to-spacing ratio, *d/s*, of 0.2. The wicking front position is measured in the middle of two adjacent pillars perpendicular to the wicking direction and plotted over two consecutive pillar spacings along the wicking direction, and $t = 0$ is defined here when the wicking front touches the row of pillars located at $a = 6$ mm both with and without nanorods. A two-stage wicking dynamic is observed in this zoomed-in experiment, where the wicking speed, i.e., the slope of the wicking position over time, is faster while around pillars but slows down as the wicking front moves in-between two adjacent pillar rows both with and without nanorods. Figure 5a shows the snapshots of the wicking front positions at three different times for the micropillar-only case, where the wicking front is uneven while around pillars. It takes ≈1 ms for the wicking front to move around pillars of 10 μm in diameter, but ≈ 25 ms to move the next 40 μm in-between two pillar rows until the front touches the next pillar row for the bare micropillar case. This slower wicking stage between two pillar rows is believed to be due to its smaller pre-wet surface area per wicking length as compared to the first wicking stage, resulting in a weaker driving force in the system free energy. As the wicking front touches the next row of pillars, the two-stage wicking cycle repeats itself. Figure 5b shows the snapshots of the bulk wicking front, marked with a red arrow, and the nano wicking front inside the nanorod region, marked with a blue arrow, at three different times for the hierarchical surface. A side-view schematic on the top row of Fig. 5b depicts the locations of the bulk and nano wicking fronts. It takes ≈ 1 ms for the bulk wicking front to move around pillars, but ≈ 17 ms to touch the next pillar row, 8 ms shorter than that of the bare micropillar case. In other words, the effect of nanorods on wicking improvement is not observable in the first (fast) wicking stage but obvious in the second stage. This second stage dictates the wicking enhancement in hierarchical surfaces

where the microscale capillary action is slower than the nanoscale one, thus the bulk wicking speed becomes the speed-limiting factor. In an effort to identify the underlying physics of this wicking enhancement due to nanorods in-between pillar rows, Fig. 5d shows the side-view schematic of the wicking front for both micropillar and hierarchical surfaces. It is important to note that the intrinsic contact angles of water on pure silicon and ZnO nanofilm coated silicon are close to each other ($\theta \approx 4^{o}$ and $\theta \approx 5^{o}$, respectively) and assumed equal. For the hierarchical surface, the apparent contact angle of the nano-rough micropillar base plane is lower than the intrinsic contact angle of water on ZnO-coated silicon or pure silicon due to the nano wicking effect, following the relation of $\cos\theta_{\text{apparent}} - \cos\theta = (1-\phi_{s,n})(1-\cos\theta) \geq 0$ [41] and hence $\theta_{\text{apparent}} < \theta$ for any $\theta > 0$, where $\phi_{s,n}$ is the solid fraction of nanorods.[41] The lower wetting angle therefore enhances wicking of the hierarchical surface as compared to the micropillar-only case. This reduction in contact angle due to the presence of nanostructures is widely observed in droplet spreading scenarios,[42-43] where a nanoscale precursor film assists wetting.[44] As shown in Fig. 5b, a nano wicking front of ≈ 40 to 60 μm ahead of the bulk wicking is observed on the hierarchical surface.

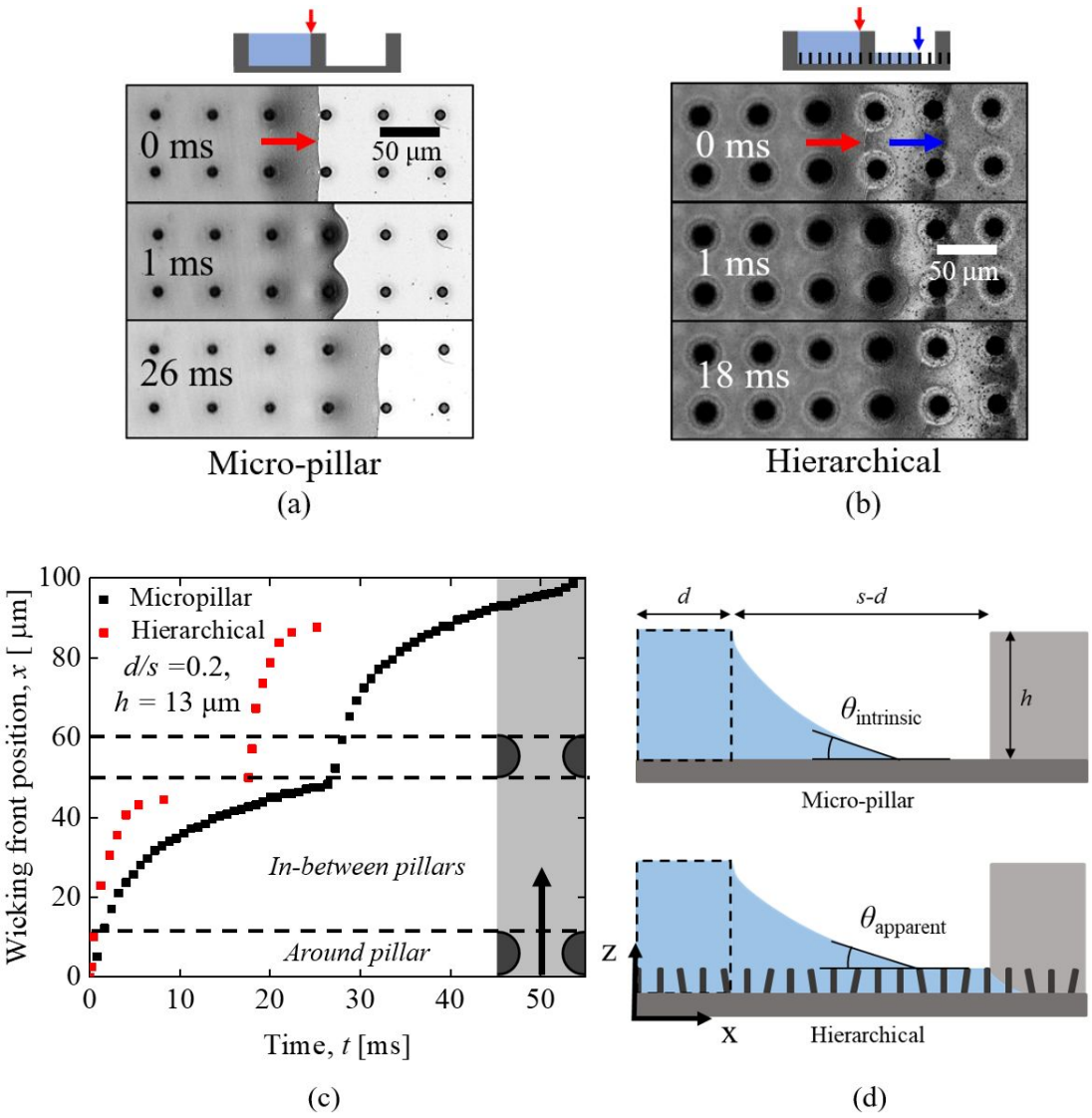

Figure 5. (a) Snapshots showing wicking front positions (red arrow) at t = 0, 1 and 26 ms when the wicking front touches the first pillar row, just passes the first pillar row, and touches the next pillar row, respectively. (b) Snapshots showing bulk (red arrow) and nano (blue arrow) wicking front positions at t = 0, 1 and 18 ms for the hierarchical surface when the bulk wicking front touches the first pillar row, just passes the first row and touches the next pillar row respectively. (c) Wicking front positions over time for micropillars (black square) and hierarchical surfaces (red square) for d/s =0.2 and h = 13 μm for two consecutive pillar spacings where the wicking front is 6 mm away from the liquid reservoir. A two-stage wicking motion is observed for both micropillar and hierarchical surfaces. (d) Schematic diagram of the wicking front between two pillar rows for micropillar-only (top) and hierarchical (bottom) surfaces.

To examine why only limited wicking improvement is observed for hierarchical surfaces of d/s = 0.333, shown in Fig. 4a, Figure 6 compares the wicking dynamics of hierarchical surfaces for d/s = 0.333 and 0.2. The bulk and nano wicking front positions are shown at three different times during one wicking cycle for both cases. The side-view schematics are shown on the top with red and blue arrows indicating the positions of the bulk and nano wicking fronts, respectively. For d/s of 0.333, shown in Fig. 6a, the nano wicking front is ahead of bulk wicking at t = 0 ms, but two wicking fronts are close to each other at t = 0.5 ms. Whereas, for the case of d/s = 0.2, shown in Fig. 6b, the nano wicking front is always ahead of bulk wicking. As identified earlier, the second (slow) wicking stage dictates the wicking improvement in hierarchical surfaces and is hence the focus of the current analysis. This second stage is analogous to the scenario of droplet spreading on nanostructured surfaces where two spreading stages are identified:[42-43] the synchronous spreading stage, where the droplet apparent contact line and the nano wicking front move at same speed, followed by a hemi-spreading stage where the apparent contact line stops but the nano wicking front continues to advance. In present study, the bulk wicking front advances faster for the d/s = 0.333 case, analogous to the synchronous spreading stage with non-distinguishable bulk and nano wicking fronts, however bulk wicking is much slower for d/s = 0.2 where hemi-spreading takes place with nano wicking ahead of the bulk wicking front. In other words, the distance between the nano and bulk wicking fronts is found be to a function of the bulk wicking speed. When the bulk wicking is faster in-between pillar rows for d/s = 0.333, the wicking capability of nanostructure cannot catch up with the bulk wicking speed, resulting in a smaller nano-wicking length ahead of bulk wicking as compared to the d/s = 0.2 case, as shown in the middle column of Fig. 6.

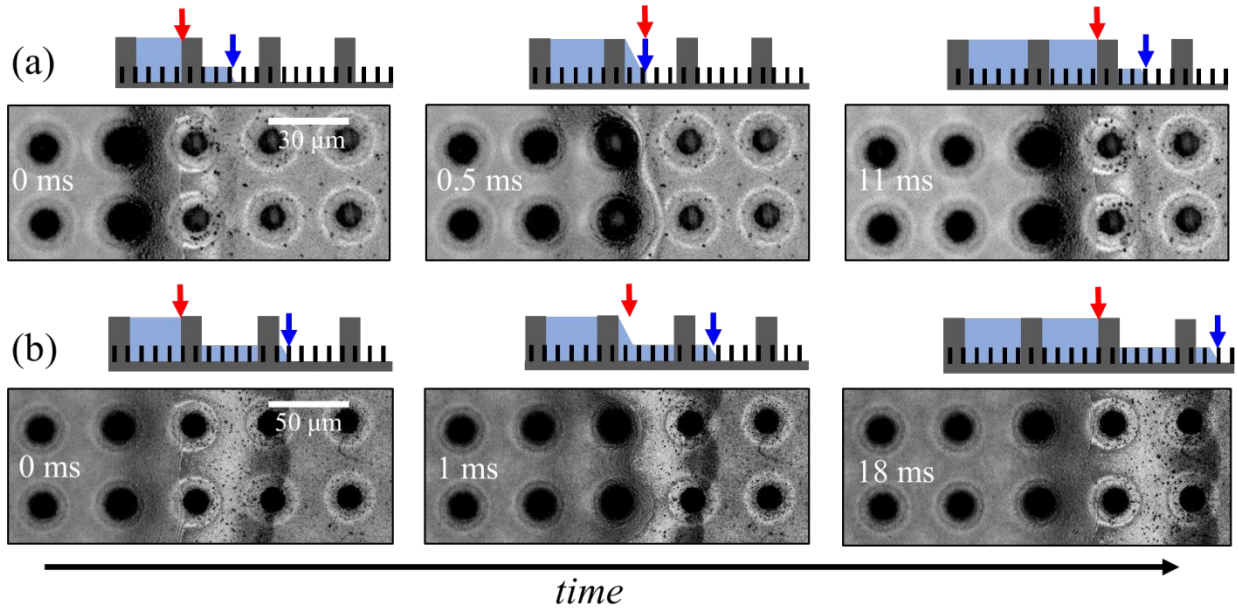

Figure 6. Bulk versus nano wicking front of the hierarchical surfaces for (a) d/s = 0.333 showing two wicking fronts close to each other at t = 0.5 ms and (b) d/s = 0.2 showing the nano wicking front ahead of the bulk wicking front at all time.

To further explore the dependence of wicking improvement on micropillar geometry, the wicking experiments were conducted on micropillars of varying height (8-26μm) and pillar-to-pillar spacing (30-60μm) without and with nanorods. Figure 7 shows the two-stage wicking dynamics for two consecutive pillar spacings for micropillar diameter-to-spacing ratio, d/s, of (a) 0.333 and (b) 0.2 both with pillar height of 26 μm. Similar to those with pillar height of 13 μm (shown in Figs. 3-6), no significant wicking enhancement is observed without and with nanorods for d/s of 0.333, shown in Fig. 7a, but obvious enhancement is observed for d/s = 0.2, shown in Fig. 7b. The bulk wicking front positions for micropillar and hierarchical surfaces are close to each other at the first wicking stage around micropillars, but the time it takes to wick in-between pillars is shorter for hierarchical surfaces compared to bare micropillars, all consistent with the findings from the h = 13 μm cases.

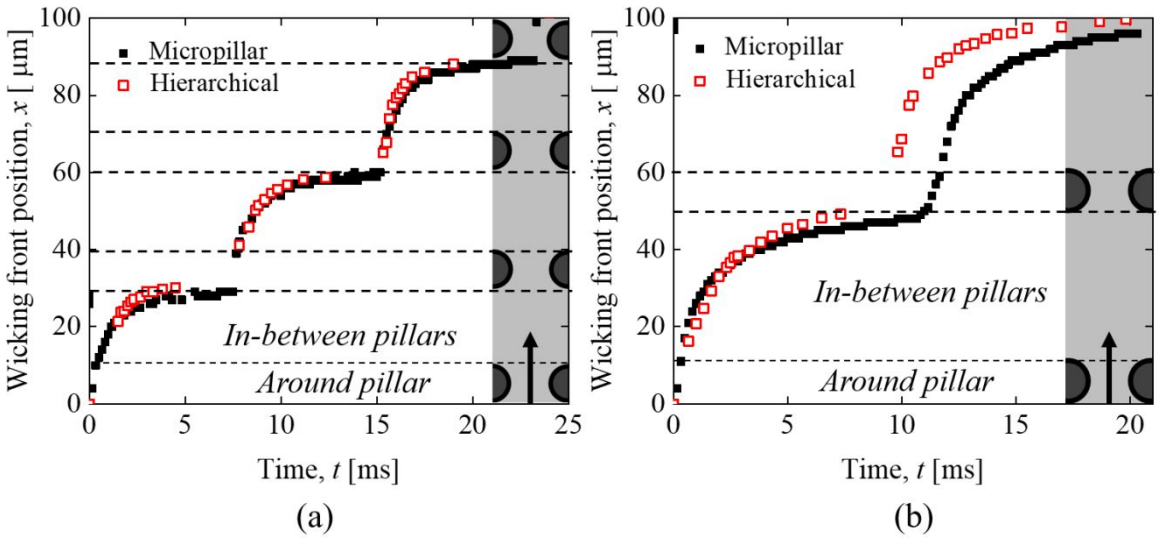

Figure 7. Comparison of wicking dynamics over two consecutive pillar spacings showing two-stage wicking dynamics on both micropillars and hierarchical surfaces for micropillar height of 26 μm and diameter-to-spacing ratio, *d/s*, of (a) 0.333 and (b) 0.2. Black and red squares are for micropillars and hierarchical surfaces, respectively.

It is important to note that, the micropillar height and pillar density are varied in this study while the nanostructures on the hierarchical surfaces are kept the same. At a relative high pillar density, e.g., d/s = 0.333, the wicking speed of the pure micropillar and hierarchical surfaces are almost the same, while at lower pillar density, e.g., d/s = 0.2, the wicking speed of hierarchical surfaces is faster. The wicking speed of the speed-limiting stage when the wicking front in between two pillar rows is increased when the pillar density of the hierarchical surface is lower. This is because the wicking front in the nanostructure is always faster than the bulk wicking front in the microstructures. The bulk wicking speed is increased in this stage by decreasing the apparent contact angle. However, the speed enhancement is negligible when the wicking front is around pillars.

4. Wicking model for hierarchical surfaces

In this section, a scaling model relating the propagation coefficient with the fluid properties

and geometrical parameters of micropillars has been developed by balancing the surface energy change with the frictional work as liquid wicks the micropillars. The model is then extended to hierarchical surfaces by incorporating the effects of nanostructures on increasing both the capillary pressure and viscous resistance.

Figure 8 depicts the systems considered in the wicking models of micropillar and hierarchical surfaces. A unit cell of micropillars consists of two distinguished regions: Region 1 is around micropillars and Region 2 is in-between pillar rows. Here, the micropillar spacing, height and diameter are shown as s, h and d, respectively. Wicking is along the x axis, pillar height is along the z axis, and y axis is perpendicular to the wicking direction. The cross-sectional view of the unit cell is shown in Fig. 8b assuming the top surface of the wicked liquid having a flat meniscus. In the model, the circular micropillars are simplified as rectangular micropillars with length d and width s-L, shown in Fig. 8c, where Region 1 is considered as a microchannel bounded by three wall surfaces: two pillar side walls and the micropillar base plane. Here, $L = \left(sd - \frac{\pi d^2}{4} \right) / d$ is the equivalent channel width of the rectangular pillars, considering Region 1 of the rectangular pillars in Fig. 8c holds the same volume of liquid as in Region 1 of the circular pillars in Fig. 8a. Note that, the length of the rectangular micropillar, along the wicking direction, is kept the same as the diameter, d, of the circular micropillar.

The following assumptions are considered in the model:

i) The meniscus shape of top surface is considered as flat during wicking and the meniscus height is the same as the height of micropillars, shown in Fig. 8b.

ii) Circular micropillars are simplified as rectangular pillars with length *d*, same as the pillar diameter, and width *s-L*, shown in Fig. 8c. Wicking in Region 1 is considered as channel flow bounded by three surfaces and in Region 2 is over a flat surface.

iii) Flow in both Region 1 and 2 is considered fully developed.

iv) Surface contamination and defects are not considered in the model.

v) Gravitational effects are not considered since the Bond number, $\mathrm{Bo} = \rho h^2 g / \gamma$[33], is very small O($10^{-6}$~$10^{-5}$).

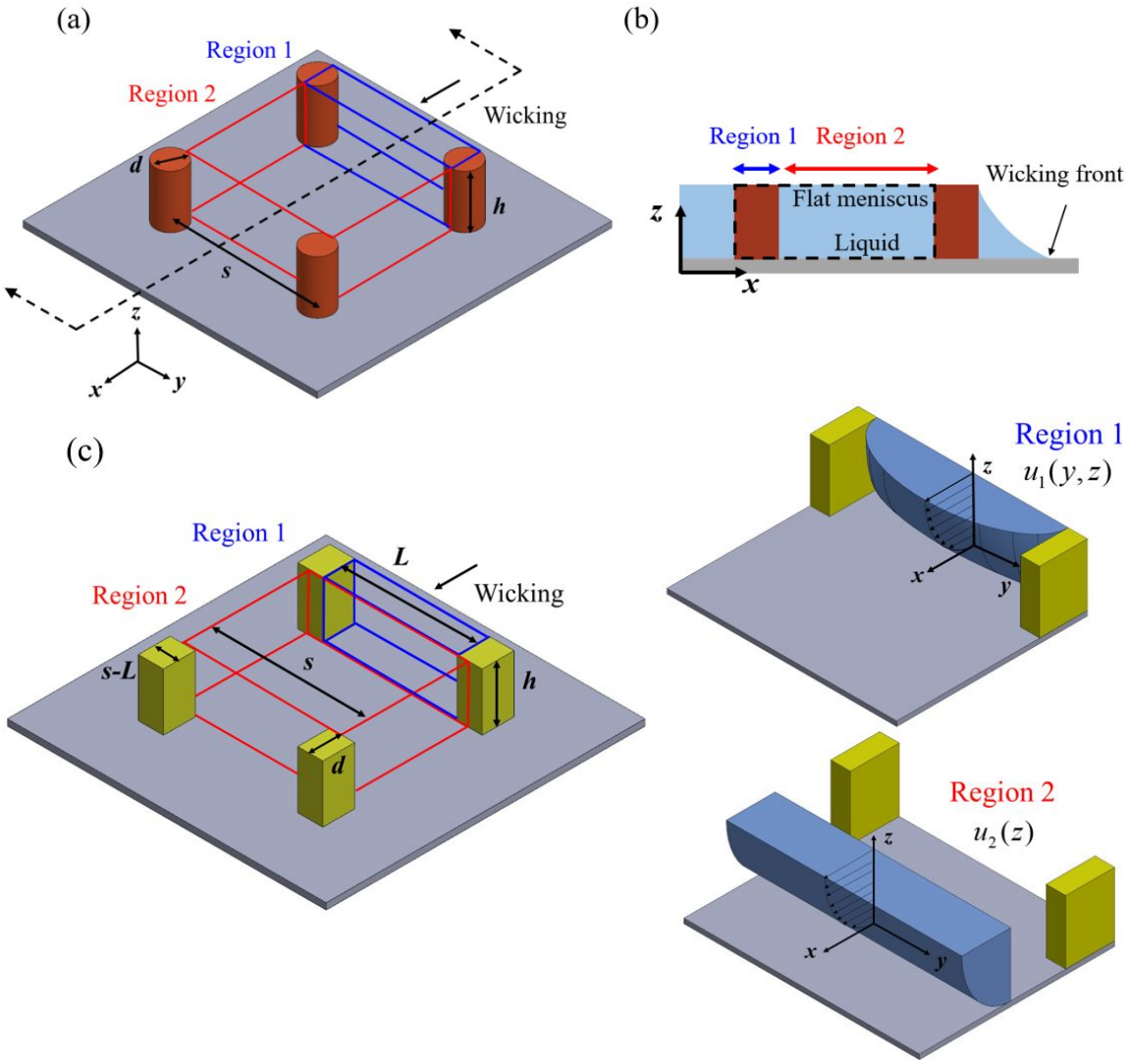

Figure 8. (a) A unit cell of the structured surface consisting of two distinguished wicking regions: the blue box is Region 1 (around micropillars) and the red box is Region 2 (in-between pillar rows). (b) cross-sectional view of the structure along the wicking direction *x*, showing the flat meniscus on the top as assumed in the current study. Black dashed box is one unit-cell, consisting of regions 1 and 2. (c) Wicking in circular micropillars is simplified as wicking in rectangular micropillars with length *d* and width *s-L*, where Region 1 is bounded by three wall surfaces, holding the same volume of liquid as Region 1 around circular micropillars shown in (a). Schematic of the velocity profiles in Region 1 and 2 are shown where $u_1(y,z)$ is the *x*-velocity of the wicking liquid in Region 1 (bounded by three wall surfaces) and $u_2(z)$ is the *x*-velocity in Region 2 (over the micropillar base plane). Wicking in hierarchical surfaces is modeled assuming nanostructures in both Region 1 and 2.

The model is based on balancing the total work done to overcome the frictional resistances as liquid wicks from the water bath level to the wicking front with the change in surface energy of the system as liquid wicks over one-unit cell, expressed as $\frac{a}{s}W_{\text{total}} = \Delta E$, where a is the wicking length, W_{total} is the work done to overcome frictional resistance for one unit-cell of length, s. The change in surface energy of the system as liquid wicks over one-unit cell of the micropillar surface consists of Region 1 and 2, as shown in Fig. 8a, is given by

$$\Delta E = \gamma\left[\left(r_m - \phi_{s,m}\right)\cos\theta - (1-\phi_{s,m})\right]s^2 \tag{1}$$

where $r_m = 1 + \frac{\pi dh}{s^2}$ is the roughness measure of micropillars, $\phi_{s,m} = \frac{\pi d^2}{4s^2}$ is the solid fraction of a unit cell, and θ the intrinsic contact angle.

Frictional losses arise due to liquid wicking in Region 1 and 2 of the unit cell. In Region 1, for bare micropillars, wicking flow can be considered as a channel flow, bounded by two pillar side walls and a pillar base plane, as shown in Fig. 8c. The x-velocity of the wicking flow in Region 1, u_1, depends on both y and z coordinates and can be derived assuming no-slip conditions on three side walls, i.e., $u_1(y,z) = 0$ at $y = -\frac{L}{2}$, $y = \frac{L}{2}$, and $z = 0$, and a free surface on the top, i.e., $\frac{\partial}{\partial z}\left(u_1(y,z)\right) = 0$ at $z = h$, following

$$u_1(y,z) = U_{1,\max}\left[2\left(\frac{z}{h}\right) - \left(\frac{z}{h}\right)^2\right]\left(1 - 4\left(\frac{y}{L}\right)^2\right) \tag{2}$$

Here, $U_{1,\max}$ is the maximum velocity of Region 1 at $z=h$ and $y=0$. Shear forces exerted by the no-slip walls are calculated from the velocity gradient as $F_{1,s}=2A_{1,s}\mu\left.\frac{\partial u_1}{\partial y}\right|_{y=-L/2}=2\mu d\int_0^h\left.\frac{\partial u_1}{\partial y}\right|_{y=-L/2}dz$ for side walls and $F_{1,b}=A_{1,b}\mu\left.\frac{\partial u_1}{\partial z}\right|_{z=0}=\mu d\int_{-L/2}^{L/2}\left.\frac{\partial u_1}{\partial z}\right|_{z=0}dy$ for the bottom surface, where $A_{1,s}$ is the area of the side wall and $A_{1,b}$ is the area of the base plane of Region 1. The work done to overcome the frictional resistance can be calculated by multiplying the shear force with the distance travelled by the wicking flow. For Region 1, the wicking front travels a distance *d* such that the friction work for the side walls becomes $W_{1,s}=F_{1,s}d\sim d^2\mu U_{1,\max}\frac{h}{L}$ and for the bottom surface it follows $W_{1,b}=F_{1,b}d\sim\mu U_{1,\max}d^2\frac{L}{h}$.

Flow in Region 2 can be considered flow over a flat surface with *x*-velocity u_2, shown in Fig. 8c whose profile depends on *z* only and can be derived assuming no-slip condition on the base plane ($u_2(z)=0$ at $z=0$) and a free surface on the top ($\frac{\partial}{\partial z}(u_2(z))=0$ at $z=h$), following

$$u_2(z)=U_{2,\max}\left[2\left(\frac{z}{h}\right)-\left(\frac{z}{h}\right)^2\right] \tag{3}$$

Here, $U_{2,\max}$ is the maximum velocity in Region 2 at $z=h$. The shear force exerted by the bottom surface is calculated from the velocity gradient as $F_{2,b}=A_{2,b}\mu\left.\frac{\partial u_2}{\partial z}\right|_{z=0}=s(s-d)\mu\left.\frac{\partial u_2}{\partial z}\right|_{z=0}$, where $A_{2,b}$ is the area of the base plane of Region 2 and μ is the liquid viscosity. For Region 2, the wicking flow travels a distance *s*-*d*, leading to frictional work, $W_{2,b}=F_{2,b}(s-d)\sim s(s-d)^2\mu\frac{U_{2,\max}}{h}$.

Considering the same amount of liquid is flowing from Region 1 to Region 2, i.e., $\dot{Q}_1 = \dot{Q}_2$, where $\dot{Q}$ is the volumetric flow rate, it leads to $U_{1,\text{avg}} L = U_{2,\text{avg}} s$, assuming the meniscus keeps a constant height of *h*. Here, the average velocity considering fully developed flow in Region 1 is $U_{1,\text{avg}} = \frac{1}{L}\frac{1}{h}\int_{-L/2}^{L/2}\int_{0}^{h} u_1(y,z)\, dydz = \frac{4}{9}U_{1,\max}$ and in Region 2 is $U_{2,\text{avg}} = \frac{1}{h}\int_{0}^{h} u_2(z)\, dz = \frac{2}{3}U_{2,\max}$. This leads to the relation between maximum velocities of Region 1 and 2 as $\frac{2}{3}U_{1,\max} L = U_{2,\max} s$. Thus, the total work done to overcome shear forces within one unit cell combining Region 1 and 2 can be expressed as $W_{\text{total}} = W_{1,b} + W_{1,s} + W_{2,b}$ following

$$W_{\text{total}} \sim \mu U_{2,\max}\left[\frac{s(s-d)^2}{h} + \frac{sd^2 h}{L^2} + \frac{d^2 s}{h}\right] \tag{4}$$

Introducing the microstructure roughness $r_m = 1 + \frac{\pi dh}{s^2}$, Eq. (4) becomes

$$W_{\text{total}} \sim \mu U_{2,\max}\frac{s^3}{h}\left[1 - \frac{d}{s}\left(1 - \frac{d}{s}\right) + \frac{d}{s}\left((r_m - 1)\frac{hs}{L^2}\right)\right] \tag{5}$$

Considering that $L^2 \approx s(s-d)$ for $s > d$ and $L \approx s$ and $U_{2,\max} \sim U_{2,\text{avg}}$, it yields

$$W_{\text{total}} \sim \mu U_{2,\text{avg}}\frac{s^3}{h}\left[1 - \frac{d}{s}\left(1 - \frac{d}{s}\right) + \frac{d}{s}\left((r_m - 1)\frac{h}{(s-d)}\right)\right] \tag{6}$$

As observed in the experiment, the slow wicking stage, i.e., Region 2, dictates the wicking dynamcis such that $U_{2,\text{avg}}$ can be approximated as the velocity of the wicking front, following $U_{2,\text{avg}} \approx \frac{da}{dt}$. This leads to

$$W_{\text{total}} \sim \mu \frac{da}{dt}\frac{s^3}{h}\left[1 - \frac{d}{s}\left(1 - \frac{d}{s}\right) + \frac{d}{s}\left((r_m - 1)\frac{h}{(s-d)}\right)\right] \tag{7}$$

Substituting Eqs. (1) and (7) in $\frac{a}{s}W_{\text{total}} = \Delta E$ and integrating, it follows

$$\frac{1}{s}\mu\frac{s^3}{h}\left[1-\frac{d}{s}\left(1-\frac{d}{s}\right)+\frac{d}{s}\left((r_m-1)\frac{h}{(s-d)}\right)\right]\int a\,da \sim \gamma\left[\left(r_m-\phi_{s,m}\right)\cos\theta-(1-\phi_{s,m})\right]s^2\int dt$$

and utilizing the wicking length versus time relation $a = G_{w/o}t^{1/2}$, it yields the following relation for the propagation coefficient without nanorods, $G_{w/o}$, as

$$G_{w/o} \sim I_{w/o} = \sqrt{\frac{\left(r_m-\phi_{s,m}\right)\cos\theta-(1-\phi_{s,m})}{1-\frac{d}{s}\left(1-\frac{d}{s}\right)+\frac{d}{s}\left((r_m-1)\frac{h}{(s-d)}\right)}\frac{\gamma h}{\mu}} \tag{8}$$

Equation (8) describes how the propagation coefficient for micropillars without nanorods is related to fluid properties, such as viscosity μ and surface tension γ, as well as the topography of micropillars, such as roughness r_m, solid fraction $\phi_{s,m}$, diameter d, height h, spacing s and wettability θ. Note that this scaling model for the propagation coefficient of wicking in micropillars is inspired by Kim et al.,[33] where the shear forces in two different regions are added to calculate the total viscous resistances. However, in the current study, the friction work instead of the friction forces is added to balance the change in surface free energy since forces in different regions should not be added.

The model for the propagation coefficient in micropillars is then extended for hierarchical surfaces, where nanostructure is considered in both Region 1 and 2. For a hierarchical surface, the change in the system free energy as liquid wicks one unit cell consists of Region 1 and 2 follows

$$\Delta E = \gamma\left[\left(r_n(r_m-\phi_{s,m})\right)\cos\theta-(1-\phi_{s,m})\right]s^2 \tag{9}$$

Here, r_n is the nanostructure roughness. The nanostructure is considered on the bottom surface and two side walls of Region 1, as well as the bottom surface of Region 2, such that it increases the

frictional resistance compared to bare micropillars. Considering β' as the resistance enhancement factor, the work done to overcome the frictional resistances of the bottom surface of Region 1 follows $W_{1,b}{}' \sim \beta' \mu U_{1,\max} d^2 \frac{L}{h}$ and for the side walls, $W_{1,s}{}' \sim \beta' d^2 \mu U_{1,\max} \frac{h}{L}$. Similarly, for Region 2, frictional resistances of the bottom surface can be scaled as $W_{2,b}{}' \sim \beta' s(s-d)^2 \mu \frac{U_{2,\max}}{h}$. This leads to the total work done to overcome the shear force for a hierarchical surface as

$$W_{\text{total}}{}' \sim \mu \beta' U_{2,\max} \left[\frac{s(s-d)^2}{h} + \frac{s d^2 h}{L^2} + \frac{d^2 s}{h} \right] \tag{10}$$

Equation (10) can be rewritten for hierarchical surfaces as

$$W_{\text{total}}{}' \sim \mu \beta' U_{2,\text{avg}} \frac{s^3}{h} \left[1 - \frac{d}{s}\left(1 - \frac{d}{s}\right) + \frac{d}{s}\left((r_m - 1) \frac{h}{(s-d)} \right) \right] \tag{11}$$

where the constant β' can be calculated by solving the Brinkman's equation for flow through a porous medium, i.e., $\mu \frac{d^2 u}{dz^2} - \varepsilon \frac{dP}{dx} - \mu \alpha^2 \varepsilon u = 0$, where $\frac{dP}{dx}$ is the pressure gradient driving the flow, $\varepsilon = 1 - \phi_{s,n} = 1 - \frac{\pi d_n{}^2}{4 s_n{}^2}$ is the porosity and $\frac{1}{\alpha^2} = s_n^2 \frac{\ln \phi_{s,n}^{-1/2} - 0.738 + \phi_{s,n} - 0.887 \phi_{s,n}^2 + 2.038 \phi_{s,n}^3 + o(\phi_{s,n}^4)}{4\pi}$ is the permeability of the nanorods and is valid for $\frac{d_n}{s_n} < 0.57$ [31] ($\frac{d_n}{s_n} \approx 0.2$ in the present study). Here, d_n, s_n and $\phi_{s,n}$ are the diameter, spacing and solid fraction of nanorods, respectively. All parameters in the Brinkman's equation are determined based on the nanostructure geometry obtained from the SEM images. The average velocity obtained from the Brinkman's equation is given by

$$\bar{u} = \frac{dP}{dx}\frac{1}{\alpha^2\mu}\left[\frac{1-e^{-\alpha\sqrt{\varepsilon}h_n}}{\alpha\sqrt{\varepsilon}h_n\left(e^{\alpha\sqrt{\varepsilon}h_n}+e^{-\alpha\sqrt{\varepsilon}h_n}\right)}+\frac{e^{\alpha\sqrt{\varepsilon}h_n}-1}{\alpha\sqrt{\varepsilon}h_n\left(e^{\alpha\sqrt{\varepsilon}h_n}+e^{-\alpha\sqrt{\varepsilon}h_n}\right)}-1\right] \quad (12)$$

which leads to the following expression for the viscous resistance enhancement factor, β', assuming the average velocity $\bar{u} = \frac{h_n^2}{3\beta'\mu}\frac{dP}{dx}$ taking the format of flow over a flat surface

$$\beta' = \frac{h_n^{\,2}}{3}\alpha^2 \Big/ \left[\frac{1-e^{-\alpha\sqrt{\varepsilon}h_n}}{\alpha\sqrt{\varepsilon}h_n\left(e^{\alpha\sqrt{\varepsilon}h_n}+e^{-\alpha\sqrt{\varepsilon}h_n}\right)}+\frac{e^{\alpha\sqrt{\varepsilon}h_n}-1}{\alpha\sqrt{\varepsilon}h_n\left(e^{\alpha\sqrt{\varepsilon}h_n}+e^{-\alpha\sqrt{\varepsilon}h_n}\right)}-1\right] \quad (13)$$

Equation (13) indicates that the viscous resistance enhancement factor, β', depends on the nanostructure topography, such as porosity ε, permeability $\frac{1}{\alpha^2}$ and height h_n. The propagation coefficient for micropillars with nanorods, $G_{w/}$, can hence be expressed as

$$G_{w/} \sim I_{w/} = \sqrt{\frac{r_n\left(r_m-\phi_{s,m}\right)\cos\theta-(1-\phi_{s,m})}{1-\frac{d}{s}\left(1-\frac{d}{s}\right)+\frac{d}{s}\left((r_m-1)\frac{h}{(s-d)}\right)}\frac{\gamma h}{\beta'\mu}} \quad (14)$$

Equation (14) describes how the propagation coefficient for micropillars with nanorods is related to fluid properties and micropillar topography, similar to Eq. (8), as well as nanorod topography, such as roughness r_n and β'. For the micropillar-only case, by setting $r_n = 1$ and $\beta' = 1$, Eq. (14) reduces to Eq. (8).

5. Comparison between model and experiments

In this section, the propagation coefficients predicted by the models are compared against experimental results of wicking on both micropillar and hierarchical surfaces. Figure 9a shows the experimental values of propagation coefficient, $G_{w/o,\,\mathrm{exp.}}$, with respect to the parameters of

micropillar geometries (diameter, spacing and height), material (intrinsic contact angle) and fluid properties (surface tension and viscosity), defined as $I_{w/o}$ in Eq. (8). The experimental values of the propagation coefficient for micropillars, $G_{w/o,\ \mathrm{exp.}}$, scales well with $I_{w/o}$ predicted by Eq. (8). The black dashed line in Fig. 9a is the least-square fitting with R^2 = 0.99 and its slope is the proportionality constant, which is 0.35 for the bare micropillar cases, accounting for the effects of surface defects and the assumptions made in the modeling section.

Similarly, Fig. 9b shows the experimentally determined propagation coefficients for the hierarchical surfaces, $G_{w/,\ \mathrm{exp.}}$, with respect to the parameters of micropillar geometries (diameter, spacing and height), material (intrinsic contact angle), nanorod geometries (diameter, spacing and height) and fluid properties (surface tension and viscosity), defined as $I_{w/}$ in Eq. (14). Good linearity is obtained between $G_{w/,\ \mathrm{exp.}}$ and $I_{w/}$ for the hierarchical surface with the red dashed fitting line in Fig. 9b corresponding to R^2 = 0.99 and its slope is the proportionality constant, which is 0.94 in the present study.

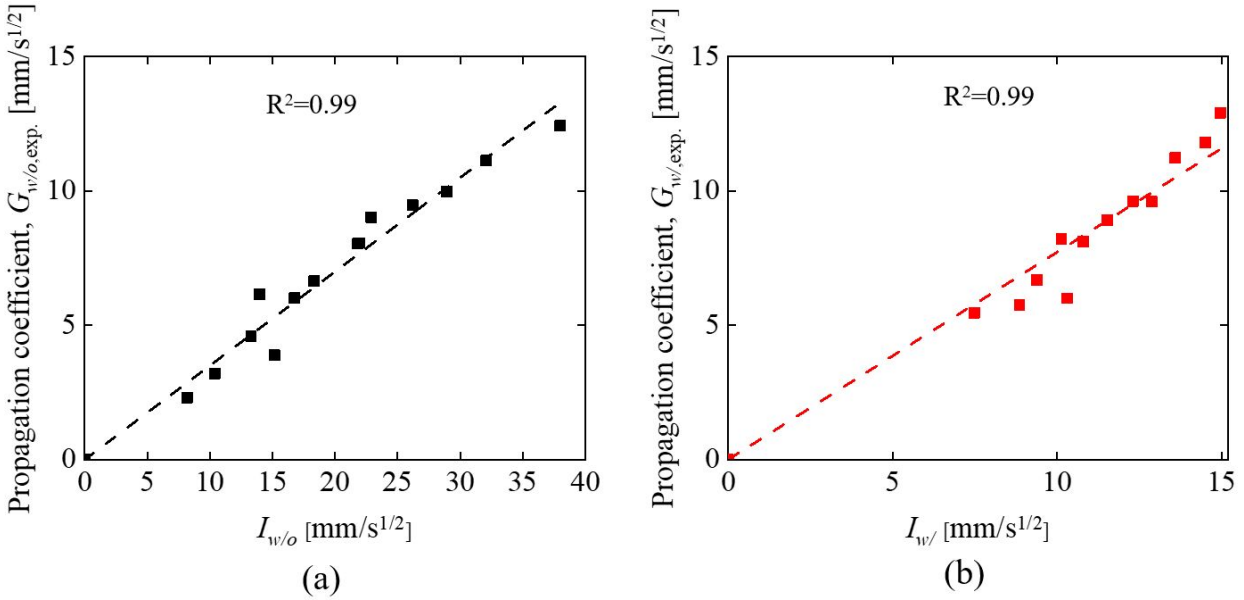

Figure 9. Experimental values of propagation coefficients, $G_{\text{exp.}}$, for wicking on (a) micropillar and (b) hierarchical surfaces are plotted against model predicted I obtained from Eq. (8) and (14) respectively, with good linearity.

The height of the micropillars is also varied in the present study and the results show that the wicking improvement of hierarchical surfaces over micropillars depends on the micropillar height. Figure 10 shows the hierarchical to micropillar propagation coefficient ratio as a function of the micropillar diameter-to-spacing ratio for different micropillar heights with symbols denoting the experimental results and lines for model predictions determined using Eqs. (8) and (14) with the proportionality constants obtained from linear fitting. Wicking enhancement in hierarchical surfaces is only observed when the ratio is higher than unity. Experimental results show that for a fixed diameter-to-spacing ratio, such as *d/s* = 0.2, wicking enhancement increases with the decrease of micropillar height, consistent with model predictions. Agreement between experiments and the model is also obtained for a certain micropillar height. For all the micropillar heights, wicking enhancement is found to be a strong function of the micropillar diameter-to-spacing ratio. The smaller the *d/s* ratio or the larger the pillar-to-pillar spacing, the stronger the enhancement. This is consistent with our two-stage wicking model: for a larger pillar-to-pillar spacing, the length of the slow wicking stage (Region 2) increases such that the effect of nanostructure wicking is more significant. Figure 10 also shows that, the higher the micropillar height or the smaller the diameter-to-spacing ratio the stronger the bulk wicking in hierarchical surfaces and smaller the wicking enhancement when compared with bare micropillars. Thus, the relative positions of nano and bulk wicking fronts or nanostructure wicking dynamics in the two wicking stages is crucial in determining the wicking enhancement in hierarchical surfaces. It is important to note that, for a high height, *h*, and a large *d/s* ratio, the hierarchical surface may experience wicking suppression as compared to micropillars alone, due to the increased friction losses of nanorods as a result of a

higher bulk wicking speed for high, dense pillars. The results also show large discrepancies between the model predictions and experiments for shorter pillars, mainly due to the actual meniscus shape during wicking deviating from the model assumption of a flat meniscus having the same height as the pillars.

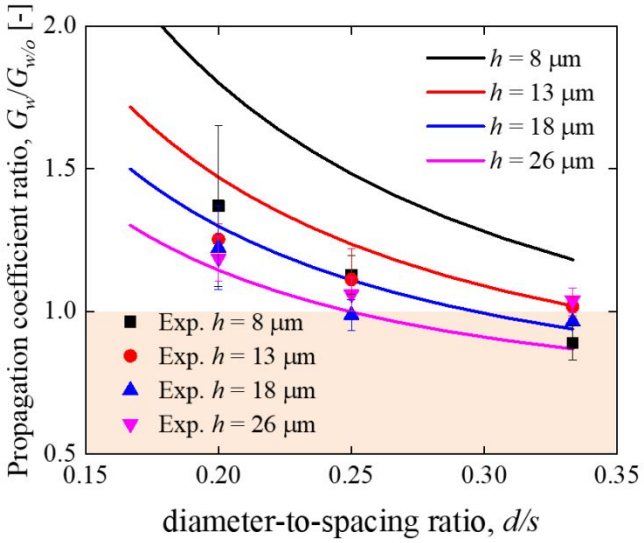

Figure 10. Comparison of hierarchical to micropillar propagation coefficient ratio between the scaling model (lines) and experiments (symbols) as a function of the diameter-to-spacing ratio for different heights of micropillars.

6. Conclusion

In this study, the role of micropatterns in two-stage wicking dynamics of hierarchical surfaces has been studied by changing the micropillar geometry (e.g., pillar spacing and height) while keeping nanostructures the same. Wicking improvement in hierarchical surfaces over micropillars is found to highly depend on the micropillar geometry. The added capillary action due to nanostructures is found to be trivial when the wicking front moves around pillars where the microscopic capillary driving force is strong, but significantly helps the wicking process when the wicking front moves in between pillar rows with a weaker microscopic capillary force. Wicking enhancement in hierarchical surfaces is related to the relative positions of the bulk and nano

wicking fronts, which determine the apparent dynamic contact angle, and is found to be more obvious for the cases of larger pillar-to-pillar spacing. Hence, adding nanostructures to existing microstructures for wicking enhancement is expected to be more effective for sparse microstructures.

Acknowledgement

Support for this work was provided by the US National Science Foundation under Grant No. CBET-1357918 and CBET-1705745.

References

1. Chu, K.-H.; Soo Joung, Y.; Enright, R.; Buie, C. R.; Wang, E. N., Hierarchically structured surfaces for boiling critical heat flux enhancement. *Applied Physics Letters* **2013,** *102* (15), 151602.
2. Dhillon, N. S.; Buongiorno, J.; Varanasi, K. K., Critical heat flux maxima during boiling crisis on textured surfaces. *Nature communications* **2015,** *6*.
3. Nam, Y.; Sharratt, S.; Byon, C.; Kim, S. J.; Ju, Y. S., Fabrication and characterization of the capillary performance of superhydrophilic Cu micropost arrays. *Journal of Microelectromechanical Systems* **2010,** *19* (3), 581-588.
4. Nam, Y.; Sharratt, S.; Cha, G.; Ju, Y. S., Characterization and modeling of the heat transfer performance of nanostructured Cu micropost wicks. *Journal of Heat Transfer* **2011,** *133* (10), 101502.
5. Oshman, C.; Li, Q.; Liew, L.-A.; Yang, R.; Lee, Y.; Bright, V. M.; Sharar, D. J.; Jankowski, N. R.; Morgan, B. C., Thermal performance of a flat polymer heat pipe heat spreader under high acceleration. *Journal of Micromechanics and Microengineering* **2012,** *22* (4), 045018.
6. Rahman, M. M.; Olceroglu, E.; McCarthy, M., Role of wickability on the critical heat flux of structured superhydrophilic surfaces. *Langmuir* **2014,** *30* (37), 11225-11234.
7. Andrews, H.; Eccles, E.; Schofield, W.; Badyal, J., Three-dimensional hierarchical structures for fog harvesting. *Langmuir* **2011,** *27* (7), 3798-3802.
8. Koch, K.; Barthlott, W., Superhydrophobic and superhydrophilic plant surfaces: an inspiration for biomimetic materials. *Philosophical Transactions of the Royal Society of London A: Mathematical, Physical and Engineering Sciences* **2009,** *367* (1893), 1487-1509.
9. Guillaume, D.; DeVries, D., Improving the pneumatic nebulizer by shaping the discharge of the capillary wick. *Journal of biomedical engineering* **1991,** *13* (6), 526-528.
10. Pararas, E. E. L.; Borkholder, D. A.; Borenstein, J. T., Microsystems technologies for drug delivery to the inner ear. *Advanced drug delivery reviews* **2012,** *64* (14), 1650-1660.
11. Araújo, A. C.; Song, Y.; Lundeberg, J.; Ståhl, P. L.; Brumer III, H., Activated paper surfaces for the rapid hybridization of DNA through capillary transport. *Analytical chemistry* **2012,** *84* (7), 3311-3317.
12. Lankelma, J.; Nie, Z.; Carrilho, E.; Whitesides, G. M., based analytical device for electrochemical flow-injection analysis of glucose in urine. *Analytical chemistry* **2012,** *84* (9), 4147-4152.

13. Liu, C.; Mauk, M. G.; Hart, R.; Qiu, X.; Bau, H. H., A self-heating cartridge for molecular diagnostics. *Lab on a Chip* **2011,** *11* (16), 2686-2692.
14. Sun, M.-H.; Huang, S.-Z.; Chen, L.-H.; Li, Y.; Yang, X.-Y.; Yuan, Z.-Y.; Su, B.-L., Applications of hierarchically structured porous materials from energy storage and conversion, catalysis, photocatalysis, adsorption, separation, and sensing to biomedicine. *Chemical Society Reviews* **2016,** *45* (12), 3479-3563.
15. Feng, X.; Jiang, L., Design and creation of superwetting/antiwetting surfaces. *Advanced Materials* **2006,** *18* (23), 3063-3078.
16. Washburn, E. W., The Dynamics of Capillary Flow. *Physical Review* **1921,** *17* (3), 273-283.
17. Yang, J.; Luo, F.; Kao, T. S.; Li, X.; Ho, G. W.; Teng, J.; Luo, X.; Hong, M., Design and fabrication of broadband ultralow reflectivity black Si surfaces by laser micro/nanoprocessing. *Light: Science & Applications* **2014,** *3* (7), e185.
18. Jeong, H. E.; Kwak, M. K.; Park, C. I.; Suh, K. Y., Wettability of nanoengineered dual-roughness surfaces fabricated by UV-assisted capillary force lithography. *Journal of colloid and interface science* **2009,** *339* (1), 202-207.
19. Fusi, M.; Di Fonzo, F.; Casari, C.; Maccallini, E.; Caruso, T.; Agostino, R.; Bottani, C.; Li Bassi, A., Island organization of Tio2 hierarchical nanostructures induced by surface wetting and drying. *Langmuir* **2011,** *27* (5), 1935-1941.
20. Mai, T. T.; Lai, C. Q.; Zheng, H.; Balasubramanian, K.; Leong, K.; Lee, P.; Lee, C.; Choi, W., Dynamics of wicking in silicon nanopillars fabricated with interference lithography and metal-assisted chemical etching. *Langmuir* **2012,** *28* (31), 11465-11471.
21. Wang, Z.; Zhao, J.; Bagal, A.; Dandley, E. C.; Oldham, C. J.; Fang, T.; Parsons, G. N.; Chang, C.-H., Wicking enhancement in three-dimensional hierarchical nanostructures. *Langmuir* **2016,** *32* (32), 8029-8033.
22. Sojoudi, H.; Kim, S.; Zhao, H.; Annavarapu, R. K.; Mariappan, D.; Hart, A. J.; McKinley, G. H.; Gleason, K. K., Stable Wettability Control of Nanoporous Microstructures by iCVD Coating of Carbon Nanotubes. *ACS applied materials & interfaces* **2017,** *9* (49), 43287-43299.
23. Choi, J.; Cho, W.; Jung, Y. S.; Kang, H. S.; Kim, H.-T., Direct fabrication of micro/nano-patterned surfaces by vertical-directional photofluidization of azobenzene materials. *ACS nano* **2017,** *11* (2), 1320-1327.
24. Wang, N.; Yuan, Y.; Wu, Y.; Hang, T.; Li, M., Wetting Transition of the Caterpillar-Like Superhydrophobic Cu/Ni–Co Hierarchical Structure by Heat Treatment. *Langmuir* **2015,** *31* (39), 10807-10812.
25. Su, B.; Tian, Y.; Jiang, L., Bioinspired interfaces with superwettability: from materials to chemistry. *Journal of the American Chemical Society* **2016,** *138* (6), 1727-1748.
26. Drelich, J.; Chibowski, E.; Meng, D. D.; Terpilowski, K., Hydrophilic and superhydrophilic surfaces and materials. *Soft Matter* **2011,** *7* (21), 9804-9828.
27. Han, J.; Cai, M.; Lin, Y.; Liu, W.; Luo, X.; Zhang, H.; Wang, K.; Zhong, M., Comprehensively durable superhydrophobic metallic hierarchical surfaces via tunable micro-cone design to protect functional nanostructures. *RSC Advances* **2018,** *8* (12), 6733-6744.
28. Bico, J.; Tordeux, C.; Quéré, D., Rough wetting. *EPL (Europhysics Letters)* **2001,** *55* (2), 214.
29. Ishino, C.; Reyssat, M.; Reyssat, E.; Okumura, K.; Quere, D., Wicking within forests of micropillars. *EPL (Europhysics Letters)* **2007,** *79* (5), 56005.
30. Brakke, K. A., The surface evolver. *Experimental mathematics* **1992,** *1* (2), 141-165.
31. Xiao, R.; Enright, R.; Wang, E. N., Prediction and optimization of liquid propagation in micropillar arrays. *Langmuir* **2010,** *26* (19), 15070-15075.
32. Kwon, H.-m.; Bird, J. C.; Varanasi, K. K., Increasing Leidenfrost point using micro-nano hierarchical surface structures. *Applied Physics Letters* **2013,** *103* (20), 201601.

33. Kim, J.; Moon, M.-W.; Kim, H.-Y., Dynamics of hemiwicking. *Journal of Fluid Mechanics* **2016,** *800*, 57-71.
34. Ahn, H. S.; Jo, H. J.; Kang, S. H.; Kim, M. H., Effect of liquid spreading due to nano/microstructures on the critical heat flux during pool boiling. *Applied Physics Letters* **2011,** *98* (7), 071908.
35. Chu, K.-H.; Enright, R.; Wang, E. N., Structured surfaces for enhanced pool boiling heat transfer. *Applied Physics Letters* **2012,** *100* (24), 241603.
36. Wu, A. H.; Cho, K.; Liaw, I. I.; Moran, G.; Kirby, N.; Lamb, R. N., Hierarchical surfaces: an in situ investigation into nano and micro scale wettability. *Faraday discussions* **2010,** *146*, 223-232.
37. Liu, B.; Cao, Z.; Zhang, Y.; Wu, Z.; Pham, A.; Wang, W.; Yan, Z.; Wei, J.; Sundén, B., Pool boiling heat transfer of N-pentane on micro/nanostructured surfaces. *International Journal of Thermal Sciences* **2018,** *130*, 386-394.
38. Son, H. H.; Kim, S. J., Role of receding capillary flow correlating nano/micro scale surface roughness and wettability with pool boiling critical heat flux. *International Journal of Heat and Mass Transfer* **2019,** *138*, 985-1001.
39. Baxter, J. B.; Walker, A.; Van Ommering, K.; Aydil, E., Synthesis and characterization of ZnO nanowires and their integration into dye-sensitized solar cells. *Nanotechnology* **2006,** *17* (11), S304.
40. Huczko, A.; Dąbrowska, A.; Madhup, D.; Subedi, D.; Chimouriya, S., Al‐doped ZnO nanofilms: Synthesis and characterization. *physica status solidi (b)* **2010,** *247* (11‐12), 3035-3038.
41. Bico, J.; Thiele, U.; Quéré, D., Wetting of textured surfaces. *Colloids and Surfaces A: Physicochemical and Engineering Aspects* **2002,** *206* (1-3), 41-46.
42. Wemp, C. K.; Carey, V. P., Water wicking and droplet spreading on randomly structured thin nanoporous layers. *Langmuir* **2017,** *33* (50), 14513-14525.
43. Chen, X.; Chen, J.; Ouyang, X.; Song, Y.; Xu, R.; Jiang, P., Water droplet spreading and wicking on nanostructured surfaces. *Langmuir* **2017,** *33* (27), 6701-6707.
44. Grewal, H.; Kim, H. N.; Cho, I.-J.; Yoon, E.-S., Role of viscous dissipative processes on the wetting of textured surfaces. *Scientific reports* **2015,** *5*, 14159.

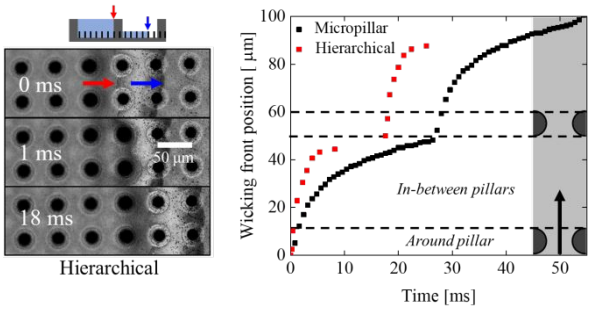

Micropattern-controlled two-stage wicking dynamics dictate the enhancement of wicking in hierarchical micro/nanostructured surfaces over bare microstructures.